

Improved analysis of neutral pion electroproduction off deuterium in chiral perturbation theory ^{*}

H. Krebs^{1 a}, V. Bernard^{2 b}, and Ulf-G. Meißner^{13 c}

¹ Helmholtz-Institut für Strahlen- und Kernphysik (Theorie), Universität Bonn, Nußallee 14-16, D-53115 Bonn, Germany

² Laboratoire de Physique Théorique, Université Louis Pasteur, F-67084 Strasbourg Cedex 2, France

³ Forschungszentrum Jülich, Institut für Kernphysik (Theorie), D-52425 Jülich, Germany

Received: date / Revised version: date

Abstract. Near threshold neutral pion electroproduction on the deuteron is studied in the framework of heavy baryon chiral perturbation theory. We include the next-to-leading order corrections to the three-body contributions. We find an improved description of the total and differential cross section data measured at MAMI. We also obtain more precise values for the threshold S-wave multipoles. We discuss in detail the theoretical uncertainties of the calculation.

PACS. 25.30.Rw Electroproduction reactions – 12.39.Fe Chiral Lagrangians – 14.20.Dh Protons and neutrons

1 Introduction

Pion electroproduction off deuterium, $\gamma^*(k) + d \rightarrow \pi^0(q) + d$, allows to extract the elusive elementary neutron amplitude. First data at small photon virtuality $k^2 = -0.1 \text{ GeV}^2$ and small values of the pion excess energy ΔW ($\Delta W = 0.5, \dots, 3.5 \text{ MeV}$) have been taken at the Mainz Mikrontron MAMI-II [1]. In the threshold region, this reaction can be analyzed in the framework of chiral perturbation theory [2, 3]. In Ref. [3], a (partial) next-to-leading order calculation was presented, which led to a satisfactory description of the differential and total cross section data. That analysis can be improved in two respects. First, the so-called three-body corrections (meson exchange currents) were only considered at third order in that paper. Second, a similar remark holds for the single scattering proton and neutron P-waves. In this paper, we are concerned with the first issue, namely the next-to-leading (fourth) order corrections to the three-body corrections. As will be shown, this introduces (in principle) no new parameters and with that extension, the calculation is done with the same theoretical precision as the fairly successful analysis of coherent neutral pion photoproduction off the deuteron [4]. It also leads to an improved description of the data as shown in this paper. The second extension can not be done so straightforwardly. This is because so far only the fourth order corrections to the photoproduction P-wave

multipoles are available in the literature [5]. For the electroproduction case, similar calculations are underway [6], triggered in particular by the rather unexpected results for neutral pion electroproduction off the proton at the photon virtuality $k^2 = -0.05 \text{ GeV}^2$ [7]. These data can not be described within chiral perturbation theory at one-loop accuracy. This is in stunning contrast to the fairly good description of the data at higher photon virtuality from NIKHEF [8] and MAMI [9] that was obtained in [10]. Note that remeasurements at the low photon virtuality seem to be more in line with expectations from chiral perturbation theory or sophisticated models [11]. As we will argue, the effect of such single scattering P-wave contributions can be effectively included in a refit of some four-nucleon-photon operators, which leads to a much improved description of the data. Given the precision of the data, a more elaborate treatment appears inappropriate.

The manuscript is organized as follows. In Section 2, we briefly discuss the pertinent formalism. We heavily borrow from Ref. [3] and only discuss the new fourth order three-body contributions in some detail. Our results are presented and discussed in Section 3 and we end with a short summary and outlook in Section 4. Some technicalities are relegated to the appendices.

2 Effective field theory description

2.1 General remarks

In Ref. [3], we developed the multipole formalism for near threshold pion electroproduction off deuterium (see also

^{*} Work supported in part by Deutsche Forschungsgemeinschaft grants Me 864/16-2 and GL 87/34-1.

^a Electronic address: h.krebs@fz-juelich.de

^b Electronic address: bernard@lpt6.u-strasbg.fr

^c Electronic address: meissner@itkp.uni-bonn.de

[12,13]) and calculated the pertinent transition matrix elements in chiral perturbation theory. This is based on an effective chiral Lagrangian of pions and nucleons chirally coupled to external sources like the photon,

$$\mathcal{L}_{\text{eff}} = \mathcal{L}_{\pi\pi} + \mathcal{L}_{\pi N} + \mathcal{L}_{NN} , \quad (1)$$

where the first term subsumes the interactions between the Goldstone bosons, the second the pion-nucleon interactions and the third term the short range part of the two-nucleon interaction. All of these Lagrangians are a series of terms with increasing chiral dimension,

$$\mathcal{L}_{\pi\pi} = \mathcal{L}_{\pi\pi}^{(2)} + \mathcal{L}_{\pi\pi}^{(4)} + \dots , \quad (2)$$

$$\mathcal{L}_{\pi N} = \mathcal{L}_{\pi N}^{(1)} + \mathcal{L}_{\pi N}^{(2)} + \dots , \quad (3)$$

$$\mathcal{L}_{NN} = \mathcal{L}_{NN}^{(0)} + \mathcal{L}_{NN}^{(2)} + \dots , \quad (4)$$

where the ellipsis stand for terms of yet higher order. The explicit expressions for the various terms are well documented in the literature, see e.g. [14]. The transition operators derived from this effective Lagrangian are then sandwiched between wave functions that were consistently generated from chiral nuclear effective field theory. The latter we take from the recent work of Ref. [15]. The various contributions can be organized in terms of a consistent power counting in terms of a small parameter q , like e.g. a meson mass, energy or nucleon three-momentum (with respect to the typical hadronic scale, say the mass of the rho meson). For a generic matrix element one has,

$$\mathcal{M} = q^\nu \mathcal{F}(q/\mu), \quad (5)$$

where μ is a renormalization scale and the function \mathcal{F} is of order one. Furthermore, ν is a counting index, i.e. the chiral dimension of any Feynman graph, for the case of pion production off nuclei, see e.g. [16]. In terms of this counting index, we include all terms with $\nu = 0$ and $\nu = -1$ (see also [3] for details).

The transition matrix elements are generated by two very different types of contributions,

$$\mathcal{M} = \mathcal{M}^{\text{ss}} + \mathcal{M}^{\text{tb}} , \quad (6)$$

where “ss” and “tb” denote the single-scattering and the three-body contribution, respectively. Here, single scattering means that the pion is emitted from the same nucleon to which the photon couples with the other nucleon acting as a mere spectator. Processes involving both nucleons are often called exchange currents, but we follow here the notation due to Weinberg [17]. At third order, all tb diagrams involve graphs with one pion in flight, whereas at the order considered here, four-nucleon contact terms with the photon absorption and pion emission from different nucleon legs come in (as discussed in more detail below). These terms can be understood from integrating out heavier mesons, see e.g. [18,19]. In such a picture, such diagrams would thus correspond to heavy meson exchange currents.

The ss terms are of course sensitive to the elementary proton and neutron electroproduction multipoles, properly boosted to the pion-deuteron center-of-mass frame

(for details, see [3]). The proton amplitude is fixed from the chiral perturbation theory study of Ref. [10]. As in our earlier work, we perform two types of fits, where we have one respectively two undetermined parameters related to the elementary $n\pi^0$ amplitude. In the fits of type 1, we have one free fifth order parameter, called a_5^n , and we include the constraint from a leading order low-energy theorem to the fourth order counterterms (as explained in [10]). The numerical value for the LEC a_3^n from resonance saturation is -4.11 GeV^{-4} (comprised of the contribution from the $\Delta(1232)$ in static approximation and vector mesons). For the fits of type 2, we relax this constraint and thus have two fit parameters, the low-energy constants a_3^n and a_4^n . These two fitting procedures give us a measure of the theoretical uncertainty at the order we are considering. We also get another measure of the theoretical uncertainty by considering chiral EFT at NNLO and varying the cut-off in the Lippmann-Schwinger equation. This will lead to bands for the various observables rather than to lines as e.g. in [3]. We will come back to this topic when discussing the results. We note already here that the uncertainty related to the two fit procedures is sizeably bigger than the one induced by the cut-off variation.

In what follows, we will use as kinematical quantities the virtuality of the photon, k^2 , which is negative in electron scattering (in the literature one often uses the positive quantity $Q^2 = -k^2$), the photon polarization ε and the pion excess energy, ΔW , that is the energy of the produced pion above threshold in the $\pi - d$ center-of-mass system. For a more detailed discussion of the kinematics, see e.g. [1].

2.2 Fourth-order three-body contributions

At third order, there are 8 tree graphs contributing to the three-body corrections, see Fig. 4 of Ref. [3] (using Coulomb gauge). At fourth order, there are altogether 59 non-vanishing diagrams, as shown in Fig. 1. These are tree graphs with exactly one insertion from the dimension two chiral pion-nucleon Lagrangian, $\mathcal{L}_{\pi N}^{(2)}$. More precisely, in that figure we have only shown the topologically inequivalent diagrams, the numbers under certain graphs denote how many diagrams can be generated if one attaches the pion emission vertex on the left or the right nucleon line above or below the pion exchange line. There is also a whole new class of short-distance diagrams including the leading (momentum-independent) four-nucleon interactions (the last four diagrams in Fig. 1 and the corresponding Okubo-corrections, i.e. the diagrams with two close-by energy denominators, are not shown. For details on this point, see [20]. A more general discussion on these re-orthonormalization diagrams can be found e.g. in [21,22]). The corresponding four-nucleon LECs have already been determined in the fits to nucleon-nucleon scattering data. We use here the values collected in table 1 for the corresponding NNLO wave functions. However, these values stem from a fit to the NN phase shifts at low energies. A fit including pion production data

LEC	$\Lambda = 450 \text{ MeV}$	$\Lambda = 650 \text{ MeV}$
$C_{1S0} [10^{-4} \text{ GeV}^{-2}]$	-0.151	-0.149
$C_{3S1} [10^{-4} \text{ GeV}^{-2}]$	-0.168	-0.130

Table 1. Values of the four-nucleon LECs for the NNLO wave functions of [15] used here. Λ is the cut-off in the Lippman-Schwinger equation (the spectral function cut-off is fixed at $\tilde{\Lambda} = 650 \text{ MeV}$)

(which is from the kinematical point of view closer to the process considered here) can lead to an increased theoretical uncertainty in the determination of these LECs. To make that point more transparent, we briefly discuss the determination of the leading $4N\pi$ LEC related to the D-term in [25]. From low-energy observables one obtains for this coupling in dimensionless units, $c_D/(F_\pi^2 \Lambda_\chi^2) = 1.8 \dots 3.6$, whereas its determination from P-waves in the reaction $pp \rightarrow pp\pi^0$ gives somewhat lower (but still consistent) values, $c_D = 1.4 \dots 2.1$ [26]¹. Also, at fourth order we will have additional P-wave LECs from the single nucleon amplitudes. With these two observations in mind, we will also perform fits were we leave C_{1S0} and C_{3S1} as free parameters. This will be discussed in more detail when we present the results. Furthermore, $\mathcal{L}_{\pi N}^{(2)}$ contains some terms with fixed couplings (due to the constraints of Lorentz invariance) and other terms with finite and scale-independent low-energy constants, denoted c_i . These LECs can e.g. be determined from the analysis of low-energy elastic pion-nucleon scattering data utilizing chiral perturbation theory. From the hadronic couplings only the term $\sim c_4$ contributes, we use the value $c_4 = 3.4 \text{ GeV}^{-1}$ [23].

We note that all the diagrams shown in Fig. 1 are irreducible, where we use the following definition for irreducible diagrams: A diagram is called irreducible, if it contains no contributions from the two-nucleon potential (see e.g. the related discussion in [24]). This definitions becomes obvious if one considers the Lippmann-Schwinger equation,

$$\begin{aligned} & \langle \phi_d \pi^0 | T | \phi_d \gamma^* \rangle = \\ & \langle \phi_d \pi^0 | (V_{\pi N} + V_{\pi NN}) + (V_{\pi N} + V_{\pi NN}) \\ & \times \frac{1}{E - H_0 - V_{NN} - V_{\pi N} - V_{\pi NN} - V_{\gamma N} - V_{\gamma NN} + i\epsilon} \\ & \times (V_{\gamma N} + V_{\gamma NN}) | \phi_d \gamma^* \rangle, \end{aligned} \quad (7)$$

and the deuteron wave function ϕ_d is obtained from the solution of the Schrödinger equation,

$$(H_0 + V_{NN}) |\phi_d\rangle = E_d |\phi_d\rangle. \quad (8)$$

Here, $V_{\pi N}, V_{\gamma N}, \dots$ are the pertinent pion-nucleon, photon-nucleon, \dots transition potentials subject to the chiral expansion as explained above. This concept of reducibility is

¹ Note that we have a different convention for the sign of the axial-vector coupling g_A . The relation between the coupling constant δ used in that paper and c_D is given by $\delta = -0.143c_D$.

depicted in Fig. 2, where two typical reducible diagrams are shown, which include either the lowest order one-pion-exchange or the short-distance parts of the two-nucleon interaction. All diagrams depicted in Fig. 1 fall essentially in four classes, labeled a), b),c) and d). The first two classes were already present at third order [3], these are the seagull-type and the pion-in-flight type graphs, respectively. Class c) collects the so-called time-ordered graphs, where the photon couples to a nucleon line and the pion is emitted from a nucleon while the exchanged pion is in flight. All diagrams build from the four-nucleon contact terms are collected in class d). Representative diagrams for these four classes are shown in Fig. 3. In fact, a) falls into two subclasses, depending on the value of the energy q'_0 of the exchanged pion. One either has $q'_0 = 0 + \mathcal{O}(1/m)$ or $q'_0 = q_0 + \mathcal{O}(1/m)$, with q_0 the energy of the produced pion. The diagrams are evaluated using Fourier-transformation techniques, as briefly discussed in App. A. We also remark that all our coordinate space integrals are finite due to the exponential fall-off of the chiral EFT wave functions. In contrast to what was done in [4], we thus do not need to introduce an additional cut-off in the fourth order tb terms.

3 Results and discussion

In this section, we display the results for the multipoles, differential and total cross sections and the S-wave cross section a_{0d} for the two fit strategies. We have performed calculations with the chiral EFT wave functions at NNLO [15] for cut-offs in the range from 450 to 650 MeV (with the spectral function cut-off $\tilde{\Lambda}$ fixed at 650 MeV, for details see [15]). Consequently, for the observables we will obtain bands rather than single line. This method of estimating the theoretical uncertainty is one of the advantages of the chiral effective field theory approach employed here. We note that at threshold we have performed the calculations in momentum and in coordinate space, which serves as a good check on the nontrivial numerical evaluation of the various integrals.

3.1 Results with fixed four-nucleon LECs

We first discuss the result obtained keeping the four-nucleon LECs C_{1S0} and C_{3S1} fixed at the values given in section 2.2. In table 2 we collect the fitted LECs related to the elementary neutron amplitude. As discussed before, we have performed two types of fits. We see from the table that the wave function dependence of the LECs is very weak, which points towards the conclusion that the pertinent matrix elements are dominated by the contributions from the long-ranged pion exchange. The resulting values are also not very different from the ones obtained in [3], which are also given in the table.

Before showing results for the pertinent observables, we discuss a few general features of the new contributions. First, we observe that the $4N$ contact interactions contribute mostly to the P-waves, their S-wave contribution

LECs	$\Lambda = 450 \text{ MeV}$	$\Lambda = 650 \text{ MeV}$	$\mathcal{O}(q^3)$
$a_3^n [\text{GeV}^{-4}]$	4.148	4.140	4.767
$a_4^n [\text{GeV}^{-4}]$	-7.085	-6.730	-5.644
$a_5^n [\text{GeV}^{-5}]$	-38.71	-37.05	-27.51

Table 2. Values of the fitted LECs for the NNLO wave functions from [15]. The values for $a_{3,4}^n$ refer to the fits 2, whereas the corresponding a_5^n belongs to the respective fits 1. For comparison, the LECs from [3] are also shown.

is very small. Further, these P-wave contributions mostly feed into the magnetic M_{10}^n multipole and cancel to some extent the corresponding contribution from the third order tb terms. Second, the other new diagrams also lead to more changes in the P-wave multipoles, simply since at this order there are no free parameters. We also note that the value of the constant a_3^n in the fits 2 agrees nicely in magnitude with the resonance saturation estimate, but comes out with opposite sign.

In Figs. 4,5 we show the differential cross sections for fits 1 and 2 employing the NNLO wave functions in comparison to the MAMI data [1]. These two bands (which are generated by utilizing the NNLO wave functions with the cut-off $\Lambda = 450 \text{ MeV}$ and 650 MeV) corresponding to the two fit procedures can be considered as a measure of the theoretical uncertainty at this order. We note that the bands due to the wave function dependence are very thin, which shows that the effective field theory calculation of these wave functions is of sufficient accuracy. The uncertainty generated from the two fit procedures is comparable to the experimental errors. We remark that the differences between the two fit procedures is somewhat smaller as it was the case when only the third order tb corrections were included [3], see the dashed lines in Figs. 4,5. Consequently, as it should be in a converging effective field theory, the theoretical uncertainty has become smaller as compared to Ref. [3], although this improvement is moderate.

The corresponding total cross sections as a function of the excess energy ΔW and of the photon polarization ε are shown in Figs. 6 for fit 1 and in Figs. 7 for fit 2 and the NNLO wave function with Λ ranging from 450 to 650 MeV, respectively. We notice that for fit 1 with increasing excess energy and, in particular, with increasing photon polarization the data are systematically below the chiral prediction. Due to the fitting procedure, the slopes of the various curves for the Rosenbluth separation shown in the right panel of Fig. 6 are of course correct. These results are very similar to the ones obtained in [3] for fit 1. We note that the predictions for fit procedure 2 are visibly improved compared to the third order calculation. This is further seen by looking at the transverse and the longitudinal threshold S-wave multipole shown in Fig. 8. The prediction for $|L_d|$ for fit 2 is now within the error bar of the MAMI result (which was not the case in [3]). We note that the real part of the predicted longitudinal amplitude is negative, consistent with our findings in [3]. The resulting S-wave cross section a_{0d} is shown in Fig. 9.

The theoretical uncertainty is a bit smaller than in case of the third order tb calculation [3].

3.2 Results with fitted four-nucleon LECs

As argued before, we will also perform fits leaving the values of the two four-nucleon LECs as free parameters. Since as we noted before these operators contribute very little to the S-waves, and not at all at threshold, the fits of type 1 are performed in two stages. First, a_5^n is adjusted to give the proper value of $|L_d|$ at $k^2 = -0.1 \text{ GeV}^2$. Then, the two four-nucleon LECs are fitted to the total cross sections. The fits of type 2 are performed as before, all parameters are fixed on the total cross sections. Having said this, we collect in table 3 the values of the various LECs for the two types of fits. We note that the four-nucleon LECs come out much larger than from the investigation of nucleon-nucleon scattering, cf. table 1. However, as we discussed earlier, leaving these LECs as free parameters effectively subsumes some effects from the single nucleon P-wave contributions, so that these fits should be considered indicative only.

LECs	$\Lambda = 450 \text{ MeV}$	$\Lambda = 650 \text{ MeV}$
$a_3^n [\text{GeV}^{-4}]$	4.500	4.751
$a_4^n [\text{GeV}^{-4}]$	-8.549	-8.573
$C_{1S0} [10^{-4} \text{ GeV}^{-2}]$	-0.589	-0.664
$C_{3S1} [10^{-4} \text{ GeV}^{-2}]$	-1.168	-1.105
$a_5^n [\text{GeV}^{-5}]$	-38.71	-37.05
$C_{1S0} [10^{-4} \text{ GeV}^{-2}]$	-0.325	-0.387
$C_{3S1} [10^{-4} \text{ GeV}^{-2}]$	-0.762	-0.890

Table 3. Values of the fitted LECs for the NNLO wave functions from [15]. The values for $a_{3,4}^n$ refer to the fits 2 with the corresponding values for C_{1S0} and C_{3S1} , whereas the corresponding a_5^n belongs to the respective fits 1, again with the corresponding four-nucleon LECs.

The resulting total cross sections are shown in Fig. 10. We observe a clear improvement for fit 1 and a very good description for fit 2. We remark, however, that the corresponding differential cross sections for $\Delta W \geq 1.5 \text{ MeV}$ are more symmetric around $\cos(\theta) = 0$ (bell-shaped) than the ones shown in the preceding section, whereas the data indicate a peaking into the backward direction. This points towards an insufficient accuracy in the description of some of the P-wave multipoles. The resulting longitudinal deuteron S-wave multipole is shown in Fig. 11. While $|E_d|$ is almost unaffected, $|L_d(k^2 = -0.1 \text{ GeV}^2)|$ for fit 2 agrees with the empirical value. Consequently, the band for the S-wave cross section is much narrower than before, cf. the right panel of Fig. 11. This is because the cross sections are much sensitive to the longitudinal S-wave amplitude due to the kinematical enhancement proportional to the longitudinal polarization $\varepsilon_L \simeq 9$, see [1].

4 Summary and outlook

In this manuscript, we have considered neutral pion electroproduction off deuterium in the framework of heavy baryon chiral perturbation theory, extending and improving upon the work presented in [3]. The salient results of this study are:

- i) We have calculated the fourth order three-body corrections. These consist of 51 one-pion exchange diagrams with exactly one insertion from the dimension two pion–nucleon Lagrangian and 8 diagrams with one insertion from the lowest order four–nucleon interaction Lagrangian. In principle, all parameters are fixed from earlier studies of pion–nucleon and nucleon–nucleon scattering. The deuteron wave functions are taken consistently from the recent chiral EFT study of [15].
- ii) As in the earlier work [3], in which the three-body corrections were only considered at third order, we have performed two types of fits to the MAMI data [1]. The results are similar to the ones found there, although we observe a moderate improvement in the theoretical uncertainty. This is most pronounced for the longitudinal S-wave multipole $|L_d|$ in fit 2. We have also considered the dependence on the deuteron wave functions related to the cut–off in the Lippmann–Schwinger equation. It turned out that this dependence is very weak. Therefore, the process is dominated by long–range pion physics and thus sensitive to the elementary $\pi^0 n$ amplitude.
- iii) We have also performed fits where we have left the four–nucleon LECs as free parameters, based on the argument that in that way one can effectively subsume new P-wave LECs from the single scattering contribution. This leads to a visibly improved description of the total cross sections and the longitudinal S–wave multipole. However, the differential cross sections come out bell-shaped, in contrast to the experimental findings [1].

In conclusion, we have further sharpened the theoretical framework to analyse neutral pion production off deuterium in a model–independent framework. It remains to be seen whether a further improved description of the data will be possible when the fourth order pion–nucleon P–wave multipoles at fourth order become available.

Acknowledgements

We thank Evgeny Epelbaum for useful comments and supplying us with the EFT wave functions.

A Fourier transformations

The diagrams are evaluated in momentum space. To calculate the pertinent matrix elements, we perform Fourier

integrations, see e.g. [4]. The typical structures to be evaluated take the form

$$\begin{aligned} & p'_{\nu 1} \dots p'_{\nu m} \Phi^*(\mathbf{p}') \\ &= \frac{1}{(2\pi)^{3/2}} \int d^3 r_1 e^{-i\mathbf{p}' \cdot \mathbf{r}_1} (-i\partial_{\nu 1}) \dots (-i\partial_{\nu m}) \phi(\mathbf{r}_1) \\ & p_{\sigma 1} \dots p_{\sigma k} \Phi(\mathbf{p}) \\ &= \frac{1}{(2\pi)^{3/2}} \int d^3 r_2 e^{i\mathbf{p} \cdot \mathbf{r}_2} (i\partial_{\sigma 1}) \dots (i\partial_{\sigma k}) \phi(\mathbf{r}_2) , \quad (\text{A.1}) \end{aligned}$$

where $p(p')$ are initial (final) state relative nucleon momenta, ϕ is the coordinate space deuteron wave function and similarly Φ denotes the momentum space wave function. As stated, we have to consider 5 classes of diagrams,

- 1) Diagrams of type a) with $q'_0 = q_0 + \mathcal{O}(1/m)$,
- 2) Diagrams of type a) with $q'_0 = \mathcal{O}(1/m)$,
- 3) Diagrams of type b),
- 4) Time-ordered diagrams of type c),
- 5) The NN-diagrams of type d).

In the following, Θ symbolizes an arbitrary spin-operator.

Consider first the diagrams 1). The momentum of the exchanged pion is

$$\mathbf{q}' = \mathbf{p} - \mathbf{p}' + \frac{\mathbf{k}}{2} + \frac{\mathbf{q}}{2} . \quad (\text{A.2})$$

From the momentum space expression for this class of diagrams, one deduces the following pertinent Fourier-transform

$$\frac{1}{q' \cdot q' + \omega_c^2 - q_0^2 - i\epsilon} = \frac{1}{4\pi} \int d^3 r e^{-i\mathbf{q}' \cdot \mathbf{r}} \frac{e^{-\delta r}}{r} , \quad (\text{A.3})$$

with

$$\delta = \omega_c \sqrt{1 - \frac{q_0^2}{\omega_c^2}} . \quad (\text{A.4})$$

Here, ω_c is the physical value of the $nn\pi^+$ and the $pp\pi^-$ threshold, respectively. So then we have to evaluate the following integrals

$$\begin{aligned} & \int d^3 p d^3 p' p'_{\nu 1} \dots p'_{\nu m} \Phi^*(\mathbf{p}') \frac{1}{q' \cdot q' + \omega_c^2 - q_0^2 - i\epsilon} \Theta \\ & \times p_{\sigma 1} \dots p_{\sigma k} \Phi(\mathbf{p}) = 2\pi^2 \int d^3 r (-i\partial_{\nu 1}) \dots (-i\partial_{\nu m}) \phi(\mathbf{r}) \\ & \times \Theta \frac{e^{-\delta r}}{r} i\partial_{\sigma 1} \dots i\partial_{\sigma k} \phi(\mathbf{r}) e^{-i(\frac{\mathbf{k}}{2} + \frac{\mathbf{q}}{2}) \cdot \mathbf{r}} . \quad (\text{A.5}) \end{aligned}$$

Next, we evaluate the diagrams 2). The momentum of the exchanged pion now is

$$\mathbf{q}' = \mathbf{p} - \mathbf{p}' + \frac{\mathbf{k}}{2} - \frac{\mathbf{q}}{2} . \quad (\text{A.6})$$

and the pertinent Fourier integral is

$$\frac{1}{q' \cdot q' + M_{\pi^+}^2 - i\epsilon} = \frac{1}{4\pi} \int d^3 r e^{-i\mathbf{q}' \cdot \mathbf{r}} \frac{e^{-M_{\pi^+} r}}{r} , \quad (\text{A.7})$$

leading to the structures

$$\begin{aligned} & \int d^3p d^3p' p'_{\nu 1} \dots p'_{\nu m} \Phi^*(\mathbf{p}') \frac{1}{q' \cdot q' + M_{\pi^+}^2 - i\epsilon} \Theta \\ & \times p_{\sigma 1} \dots p_{\sigma k} \Phi(\mathbf{p}) = 2\pi^2 \int d^3r (-i\partial_{\nu 1}) \dots (-i\partial_{\nu m}) \phi(\mathbf{r}) \\ & \times \Theta \frac{e^{-M_{\pi^+} r}}{r} i\partial_{\sigma 1} \dots i\partial_{\sigma k} \phi(\mathbf{r}) e^{-i(\frac{k}{2} - \frac{q}{2}) \cdot \mathbf{r}}. \end{aligned} \quad (\text{A.8})$$

We now consider the diagrams 3). Here, the photon couples to the pion in flight, thus we have two propagators. The momentum of the exchanged pion before the photon absorption is

$$\mathbf{q}' = \mathbf{p} - \mathbf{p}' + \frac{\mathbf{k}}{2} + \frac{\mathbf{q}}{2}, \quad (\text{A.9})$$

and after the photon absorption this momentum is changed to

$$\mathbf{q}'' = \mathbf{q}' - \mathbf{k}. \quad (\text{A.10})$$

We have two types of Fourier-transforms, these are:

$$\begin{aligned} & \frac{1}{(q'' \cdot q'' + \omega_c^2 - i\epsilon)(q' \cdot q' + \omega_c^2 - q_0^2 - i\epsilon)} \\ & = \int_0^1 dz \frac{1}{(\mathbf{l}^2 + m'^2 - i\epsilon)^2}, \end{aligned} \quad (\text{A.11})$$

with

$$\begin{aligned} \mathbf{l} & = \mathbf{q}' - z\mathbf{k}, \\ m'^2 & = \omega_c^2 z + (1-z)(\delta^2 + \mathbf{k}^2 z), \end{aligned} \quad (\text{A.12})$$

and

$$\begin{aligned} & \frac{q'_{\mu 1} q'_{\mu 2}}{(q'' \cdot q'' + \omega_c^2 - i\epsilon)(q' \cdot q' + \omega_c^2 - q_0^2 - i\epsilon)} \\ & = \int_0^1 dz \frac{1}{8\pi m'} \int d^3r e^{-i\mathbf{l} \cdot \mathbf{r}} \\ & \times (-i\partial_{\mu 1} + zk_{\mu 1})(-i\partial_{\mu 2} + zk_{\mu 2}) e^{-m' r}. \end{aligned} \quad (\text{A.13})$$

Note that this function is still square integrable. Higher order derivatives, however, can not be treated in this fashion. The corresponding integrals are thus

$$\begin{aligned} & \int d^3p d^3p' p'_{\nu 1} \dots p'_{\nu m} \Phi^*(\mathbf{p}') \\ & \times \frac{q'_{\mu 1} q'_{\mu 2}}{(q'' \cdot q'' + \omega_c^2 - i\epsilon)(q' \cdot q' + \omega_c^2 - q_0^2 - i\epsilon)} \\ & \times \Theta p_{\sigma 1} \dots p_{\sigma k} \Phi(\mathbf{p}) = \int_0^1 dz \frac{\pi^2}{m'} \int d^3r \\ & \times (-i\partial_{\nu 1}) \dots (-i\partial_{\nu m}) \phi(\mathbf{r}) \Theta (-i\partial_{\mu 1} + zk_{\mu 1}) \\ & \times (-i\partial_{\mu 2} + zk_{\mu 2}) e^{-m' r} i\partial_{\sigma 1} \dots i\partial_{\sigma k} \phi(\mathbf{r}) \\ & \times e^{-i(\frac{q}{2} - (z - \frac{1}{2})\mathbf{k}) \cdot \mathbf{r}}. \end{aligned} \quad (\text{A.14})$$

We now discuss the diagrams 4), which have the momentum transfer given either by Eq. (A.2) or by Eq. (A.6).

Due to the cancellation with the corresponding Okubo-type diagrams, no new structures as compared to the other type of diagrams appears (for a more detailed discussion on this point see [20])

Finally, we turn to the NN diagrams 5). Since these only involve contact interactions, we have to consider simple structures of the form

$$\begin{aligned} & \int d^3p d^3p' p'_{\nu 1} \dots p'_{\nu m} \Phi^*(\mathbf{p}') \Theta p_{\sigma 1} \dots p_{\sigma k} \Phi(\mathbf{p}) \\ & = (2\pi)^3 (-i\partial_{\nu 1}) \dots (-i\partial_{\nu m}) \phi(\mathbf{r}_1) \Big|_{r_1=0} \Theta \\ & \times (i\partial_{\sigma 1}) \dots (i\partial_{\sigma k}) \phi(\mathbf{r}_2) \Big|_{r_2=0} \end{aligned} \quad (\text{A.15})$$

We end this appendix with a note on how we treat the contributions arising from the exchange of nucleon 1 with nucleon 2 when calculating the pertinent amplitude, $A = A(1, 2) + (1 \leftrightarrow 2)$. The corresponding momenta of the nucleons in terms of the center-of-mass and the photon and pion momenta are

$$\begin{aligned} \mathbf{p}_1 & = \mathbf{p} - \frac{\mathbf{k}}{2}, & \mathbf{p}'_1 & = \mathbf{p}' - \frac{\mathbf{q}}{2}, \\ \mathbf{p}_2 & = -\mathbf{p} - \frac{\mathbf{k}}{2}, & \mathbf{p}'_2 & = -\mathbf{p}' - \frac{\mathbf{q}}{2}. \end{aligned} \quad (\text{A.16})$$

Under a parity transformation $\mathbf{p} \rightarrow -\mathbf{p}$ and $\mathbf{p}' \rightarrow -\mathbf{p}'$, the nucleon momenta behave as $\mathbf{p}_1 \rightarrow \mathbf{p}_2$, $\mathbf{p}_2 \rightarrow \mathbf{p}_1$, $\mathbf{p}'_1 \rightarrow \mathbf{p}'_2$, $\mathbf{p}'_2 \rightarrow \mathbf{p}'_1$, which gives

$$\begin{aligned} & \int d^3p d^3p' \Phi^*(\mathbf{p}') f(\boldsymbol{\sigma}_1, \boldsymbol{\sigma}_2, \mathbf{p}_1, \mathbf{p}_2, \mathbf{p}'_1, \mathbf{p}'_2) \Phi(\mathbf{p}) \\ & = \int d^3p d^3p' \Phi^*(\mathbf{p}') f(\boldsymbol{\sigma}_1, \boldsymbol{\sigma}_2, \mathbf{p}_2, \mathbf{p}_1, \mathbf{p}'_2, \mathbf{p}'_1) \Phi(\mathbf{p}). \end{aligned} \quad (\text{A.17})$$

Thus, matrix elements are invariant under operations of the form

$$\begin{aligned} & f(\boldsymbol{\sigma}_1, \boldsymbol{\sigma}_2, \mathbf{p}_1, \mathbf{p}_2, \mathbf{p}'_1, \mathbf{p}'_2) \rightarrow \\ & f(\boldsymbol{\sigma}_1, \boldsymbol{\sigma}_2, \mathbf{p}_2, \mathbf{p}_1, \mathbf{p}'_2, \mathbf{p}'_1). \end{aligned}$$

Consequently, the operation $(1 \leftrightarrow 2)$ need only be applied to the spin and isospin operators and leave all other quantities unchanged. Furthermore, because of isospin symmetry we only have the operators $\tau_1 \cdot \tau_2 - \tau_1^z \tau_2^z$ and $\tau_1^z \tau_2^z$, which are symmetric under the interchange $(1 \leftrightarrow 2)$. Therefore, we finally only need to change the spin indices when calculating the contributions from the exchange diagrams.

B Angular integrations

Here, we briefly discuss how to efficiently perform the angular integrations of the Fourier integrals discussed in App. A. We define the following matrices constructed from the momentum space deuteron wave functions,

$$u_{n,m}(r) = \frac{1}{r^{n+m}} \sqrt{\frac{2}{\pi}} \int_0^\infty dq q^2 u(q) (qr)^n j_m(qr),$$

$$w_{n,m}(r) = -\frac{1}{r^{n+m}} \sqrt{\frac{2}{\pi}} \int_0^\infty dq q^2 w(q) (qr)^n j_m(qr) , \quad (\text{B.1})$$

where $u(q)$ and $w(q)$ are the momentum-space S- and D-wave components of the deuteron wave function, and the $j_n(qr)$ are spherical Bessel functions. The usual coordinate space expressions can be obtained using matrix elements $u_{0,0}$ and $w_{0,2}$, i.e.

$$u_{0,0} = \frac{u(r)}{r} , \quad w_{0,2} = \frac{w(r)}{r^3} . \quad (\text{B.2})$$

This notation is particularly useful since we have to deal with derivatives of the wave functions. Using the properties of the spherical Bessel functions, one obtains the following recursion relation

$$r^2 u_{n+1,m+2}(r) - (2m+3)u_{n,m+1}(r) + u_{n+1,m}(r) = 0 . \quad (\text{B.3})$$

This allows one to express the derivatives of $u_{0,0}$ in the following way

$$\begin{aligned} u'_{0,0}(r) &= -r u_{1,1}(r) , \\ u''_{0,0}(r) &= -u_{1,1}(r) + r^2 u_{2,2}(r) , \\ u'''_{0,0}(r) &= 3r u_{2,2}(r) - r^3 u_{3,3}(r) . \end{aligned} \quad (\text{B.4})$$

Similarly, the derivatives of $w_{0,2}$ can be expressed as

$$\begin{aligned} w'_{0,2}(r) &= -\frac{1}{r} (5w_{0,2}(r) - w_{1,1}(r)) , \\ w''_{0,2}(r) &= \frac{1}{r^2} (30w_{0,2}(r) - 6w_{1,1}(r) - r^2 w_{2,2}(r)) \\ w'''_{0,2}(r) &= \frac{1}{r^3} (-210w_{0,2}(r) + 42w_{1,1}(r) \\ &\quad + 6r^2 w_{2,2}(r) + r^4 w_{3,3}(r)) . \end{aligned} \quad (\text{B.5})$$

Note that one only has to calculate diagonal matrix elements.

References

1. I. Ewald *et al.*, Phys. Lett. B **499** (2001) 238 [arXiv:nucl-ex/0010008].
2. V. Bernard, H. Krebs and U.-G. Meißner, Phys. Rev. C **61** (2000) 058201 [arXiv:nucl-th/9912033].
3. H. Krebs, V. Bernard and U.-G. Meißner, Nucl. Phys. A **713** (2003) 405 [arXiv:nucl-th/0207072].
4. S. R. Beane, V. Bernard, T. S. Lee, U.-G. Meißner and U. van Kolck, Nucl. Phys. A **618** (1997) 381 [arXiv:hep-ph/9702226].
5. V. Bernard, N. Kaiser and U.-G. Meißner, Eur. Phys. J. A **11** (2001) 209 [arXiv:hep-ph/0102066].
6. V. Bernard, B. Kubis and U.-G. Meißner, forthcoming.
7. H. Merkel *et al.*, Phys. Rev. Lett. **88** (2002) 012301 [arXiv:nucl-ex/0108020].
8. H. B. van den Brink *et al.*, Phys. Rev. Lett. **74** (1995) 3561.
9. M. O. Distler *et al.*, Phys. Rev. Lett. **80** (1998) 2294.
10. V. Bernard, N. Kaiser and U.-G. Meißner, Nucl. Phys. A **607** (1996) 379 [Erratum-ibid. A **633** (1998) 695] [arXiv:hep-ph/9601267].
11. H. Merkel, in “Chiral Dynamics: Theory and Experiment (CD2003),” U.-G. Meißner, H.-W. Hammer and A. Wirzba (eds.), arXiv:hep-ph/0311212.
12. H. Arenhövel, Few Body Syst. **25** (1998) 127 [arXiv:nucl-th/9809067].
13. H. Arenhövel, Few Body Syst. **27** (1999) 141 [arXiv:nucl-th/9907005].
14. V. Bernard, N. Kaiser and U.-G. Meißner, Int. J. Mod. Phys. E **4** (1995) 193 [arXiv:hep-ph/9501384].
15. E. Epelbaum, W. Glöckle and U.-G. Meißner, Eur. Phys. J. A **19** (2004) 401 [arXiv:nucl-th/0308010].
16. S. R. Beane, C. Y. Lee and U. van Kolck, Phys. Rev. C **52** (1995) 2914 [arXiv:nucl-th/9506017].
17. S. Weinberg, Phys. Lett. B **295** (1992) 114 [arXiv:hep-ph/9209257].
18. J. L. Friar, Few Body Syst. **22** (1997) 161 [arXiv:nucl-th/9607020].
19. E. Epelbaum, U.-G. Meißner, W. Glöckle and C. Elster, Phys. Rev. C **65** (2002) 044001 [arXiv:nucl-th/0106007].
20. H. Krebs, V. Bernard and U.-G. Meißner, forthcoming.
21. J. A. Eden and M. F. Gari, Phys. Rev. C **53** (1996) 1510 [arXiv:nucl-th/9601025].
22. E. Epelbaum, W. Glöckle and U.-G. Meißner, Nucl. Phys. A **637** (1998) 107 [arXiv:nucl-th/9801064].
23. P. Büettiker and U.-G. Meißner, Nucl. Phys. A **668** (2000) 97 [arXiv:hep-ph/9908247].
24. S. R. Beane, M. Malheiro, D. R. Phillips and U. van Kolck, Nucl. Phys. A **656** (1999) 367 [arXiv:nucl-th/9905023].
25. E. Epelbaum, A. Nogga, W. Glöckle, H. Kamada, U.-G. Meißner and H. Witala, Phys. Rev. C **66** (2002) 064001 [arXiv:nucl-th/0208023].
26. C. Hanhart, U. van Kolck and G. A. Miller, Phys. Rev. Lett. **85** (2000) 2905 [arXiv:nucl-th/0004033].
27. J.C. Bergstrom *et al.*, Phys. Rev. C **57** (1998) 3203.

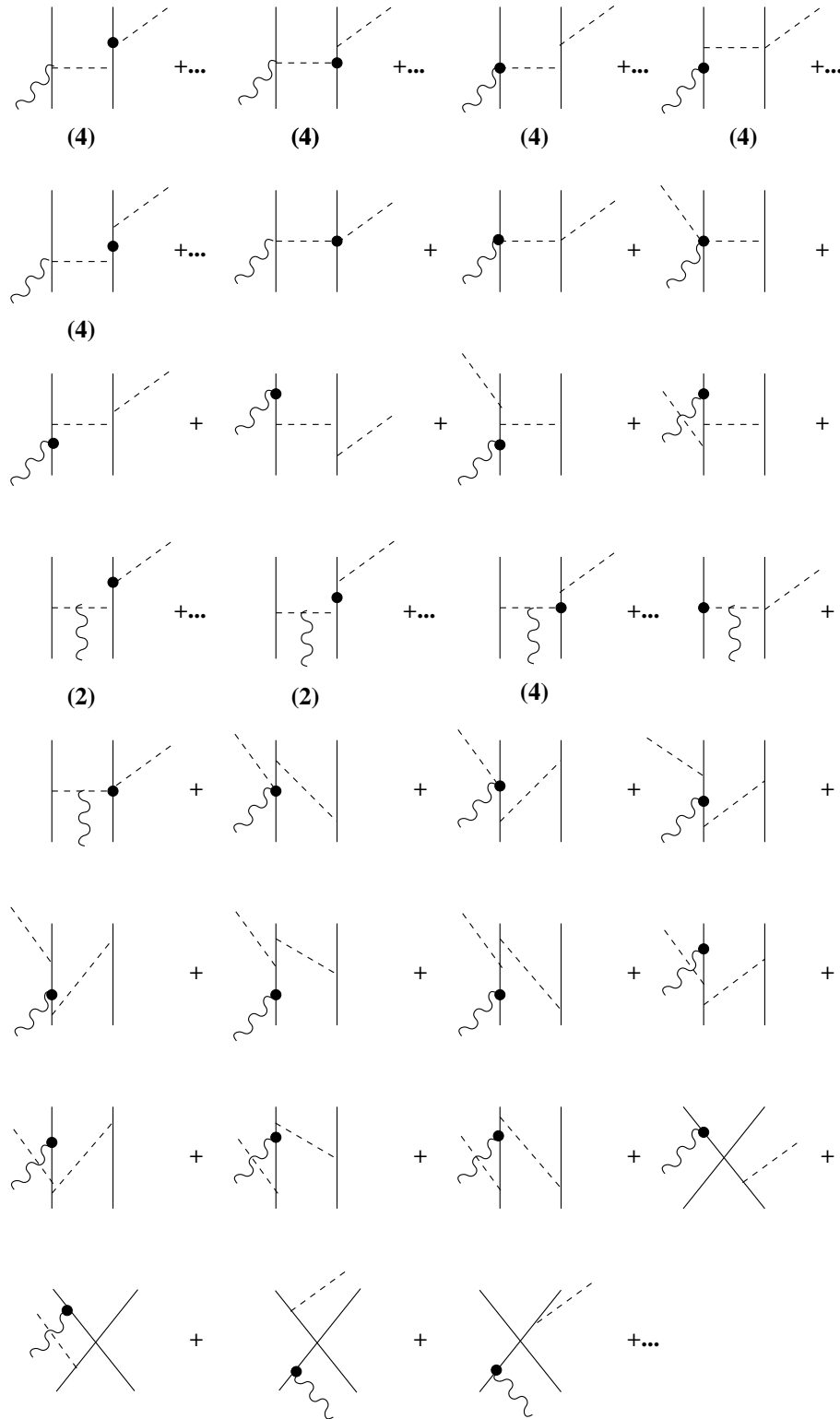


Fig. 1. Fourth order diagrams for the three-body corrections (in Coulomb gauge). Solid, dashed and wiggly lines denote nucleons, pions and photon, in order. The heavy dot stands for an insertion from the dimension two pion-nucleon Lagrangian. The number under certain graphs stands for the number of topological equivalent graphs as explained in the text. The ellipsis at the end stands for Okubo-type corrections to the graphs involving the four-nucleon contact interactions and also one-pion exchange.

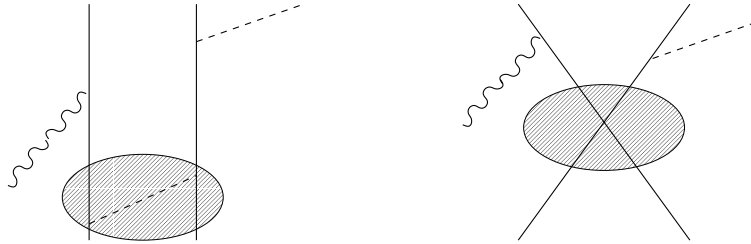


Fig. 2. Classes of reducible diagrams as explained in the text. The shaded area denotes the two-nucleon interaction, which includes either the leading one-pion exchange (left) of the momentum-independent four-nucleon interactions (right). Such types of diagrams are consistently not included in the three-body interaction kernel.

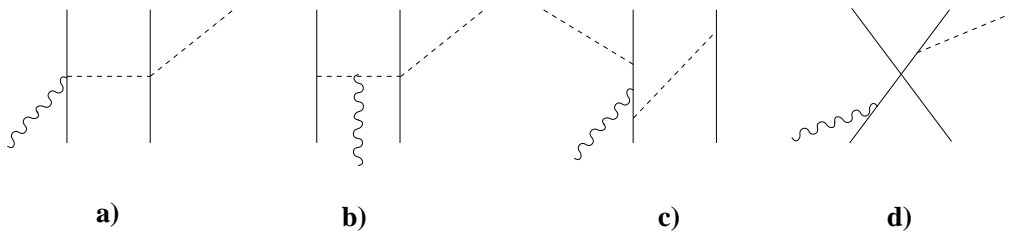


Fig. 3. Classes of irreducible diagrams as explained in the text. a) represents a seagull, b) a pion-in-flight, c) a time-ordered and d) a short-distance diagram, in order.

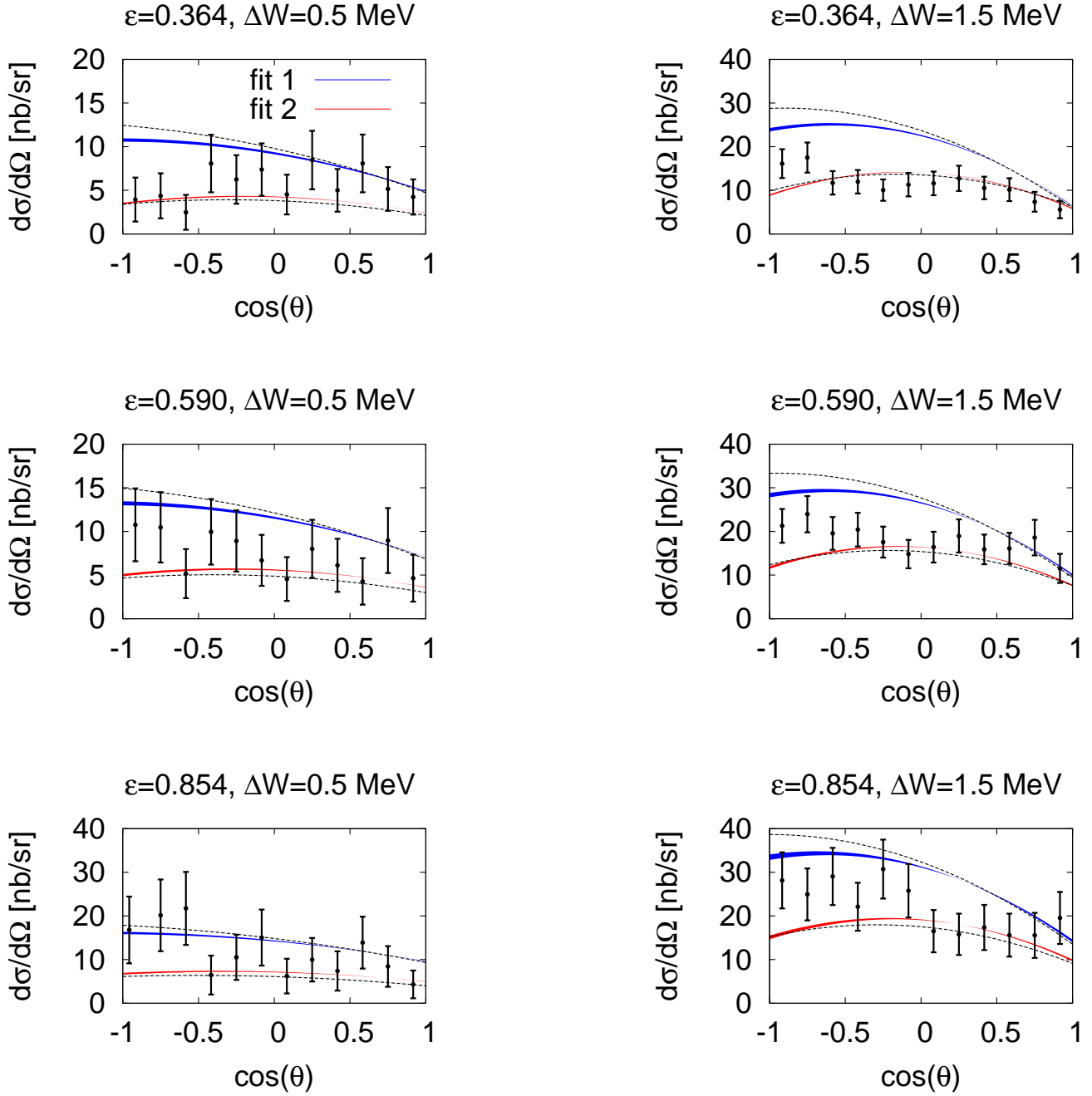


Fig. 4. Differential cross section at $\Delta W = 0.5$ MeV (left column) and $\Delta W = 1.5$ MeV (right column) at three different values of the photon polarization for the NNLO wave functions in comparison to the MAMI data [1]. Fits 1 and 2 are given by the blue (upper) and the red (lower) bands, respectively. The bands are generated by varying Λ from 450 to 650 MeV. The dashed lines are the corresponding results from [3].

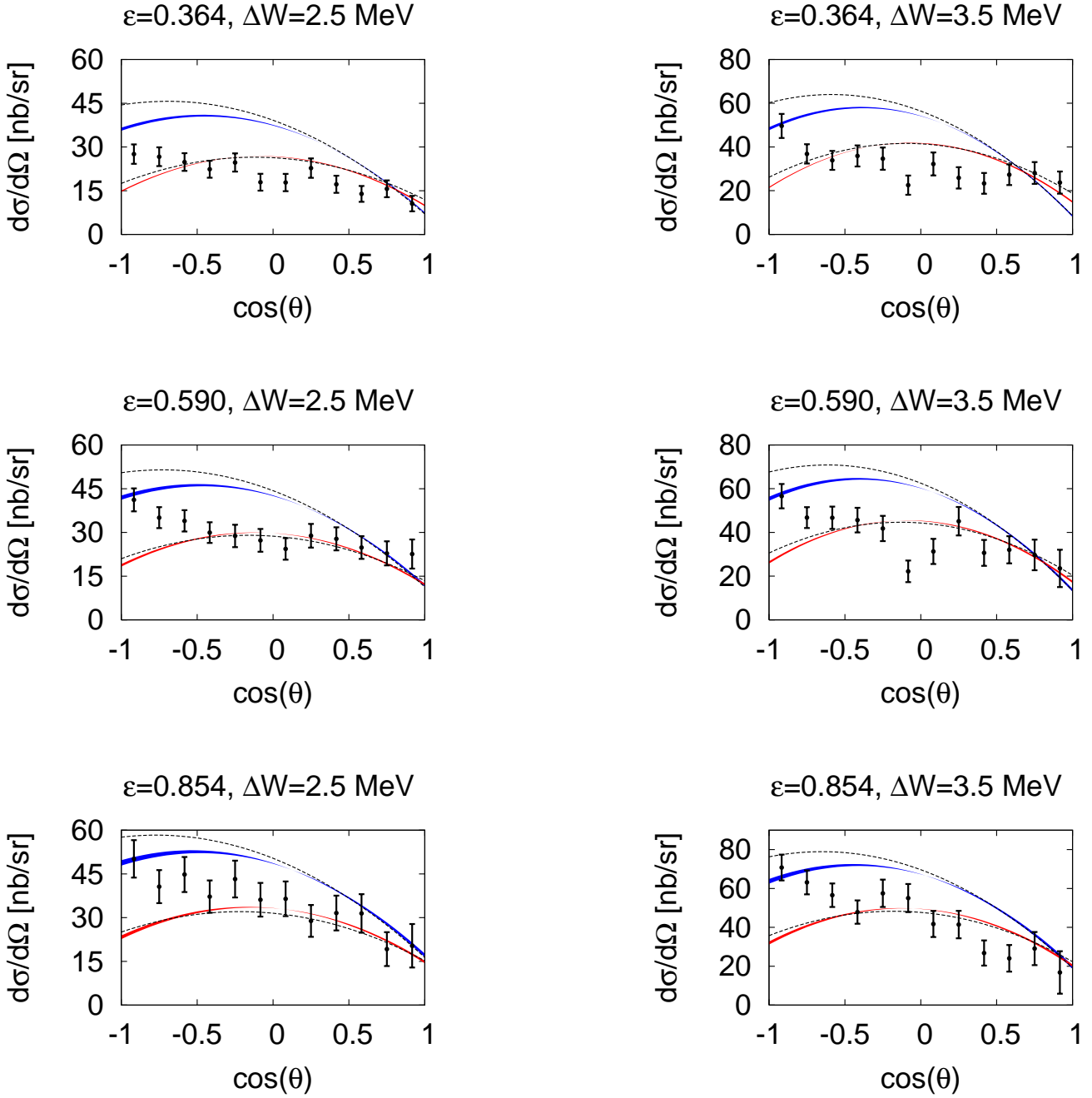


Fig. 5. Differential cross section at $\Delta W = 2.5$ MeV (left column) and $\Delta W = 3.5$ MeV (right column) at three different values of the photon polarization for the NNLO wave functions in comparison to the MAMI data [1]. Fits 1 and 2 are given by the blue (upper) and the red (lower) bands, respectively. The dashed lines are the corresponding results from [3].

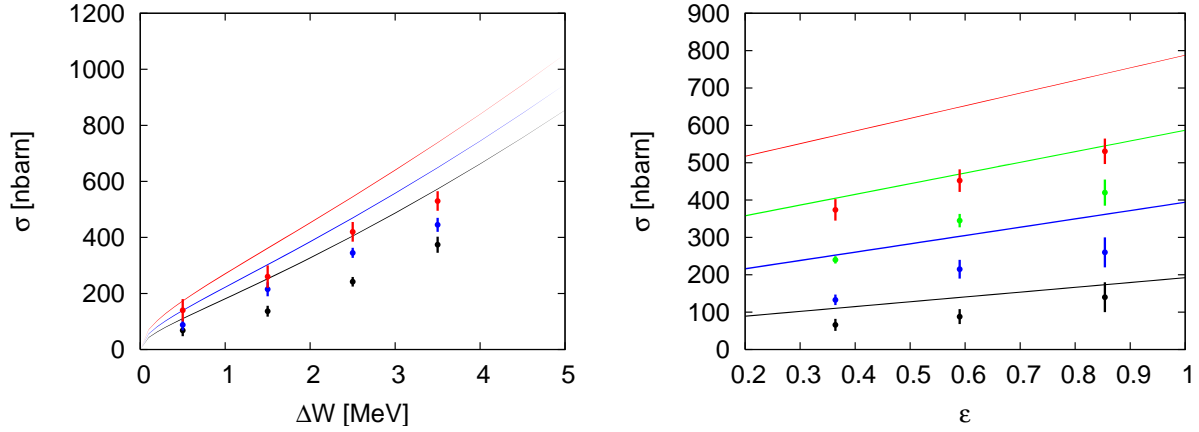


Fig. 6. Left panel: Total cross section as a function of ΔW for three different values of the photon polarization in comparison to the MAMI data [1] for fit 1 and the NNLO wave functions. The upper/middle/lower band corresponds to the largest/medium/smallest value of ε . Right panel: Total cross section as a function of the photon polarization ε for four different values of the pion excess energy ΔW . The highest band corresponds to the largest value of ΔW and correspondingly for the other bands/values of ΔW .

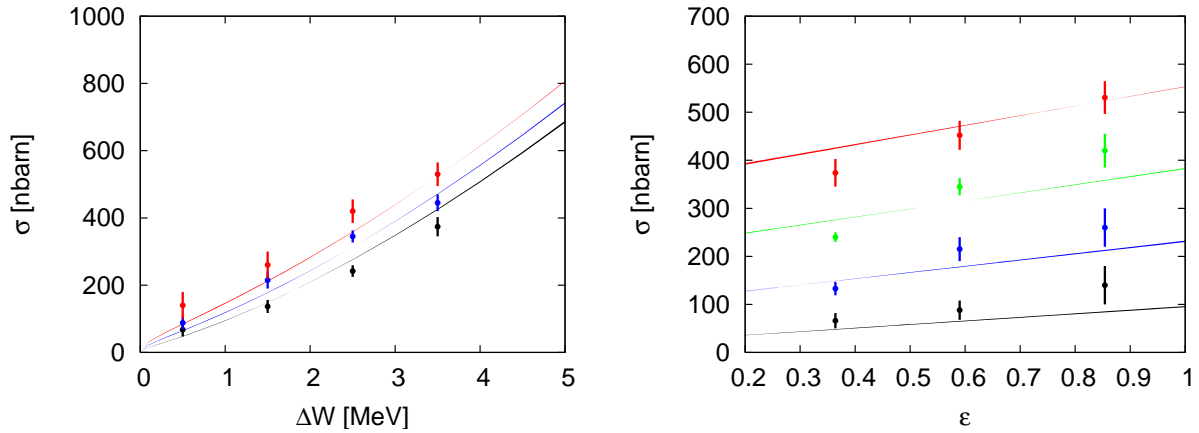


Fig. 7. Left panel: Total cross section as a function of ΔW for three different values of the photon polarization in comparison to the MAMI data [1] for fit 2 and the NNLO wave functions. The upper/middle/lower band corresponds to the largest/medium/smallest value of ε . Right panel: Total cross section as a function of the photon polarization ε for four different values of the pion excess energy ΔW . The highest band corresponds to the largest value of ΔW and correspondingly for the other bands/values of ΔW .

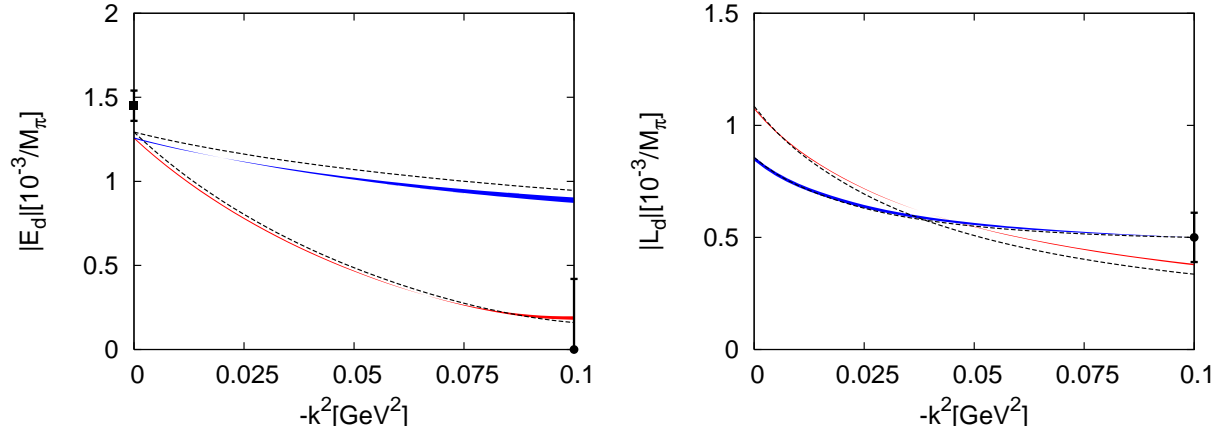


Fig. 8. Threshold multipoles $|E_d|$ (left panel) and $|L_d|$ (right panel) as a function of the photon virtuality in comparison to the photon point data from SAL [27] and the electroproduction data from MAMI [1]. The sign of the experimental result for L_d is taken to agree with the theoretical prediction. E_d : The blue (upper)/red (lower) band refers to fit 1,2, in order (for L_d , the upper/lower refers to the value at $Q^2 = 0.1 \text{ GeV}^2$). The dashed lines are the corresponding results from [3].

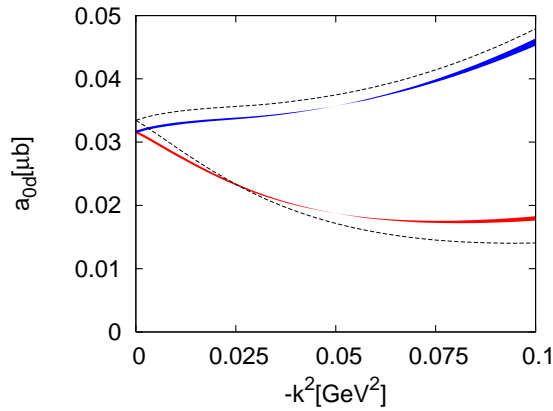


Fig. 9. The S-wave cross section a_{0d} as a function of the photon virtuality. Solid bands (dashed lines): Range obtained with the fourth (third) order three-body corrections. The dashed lines are the corresponding results from [3].

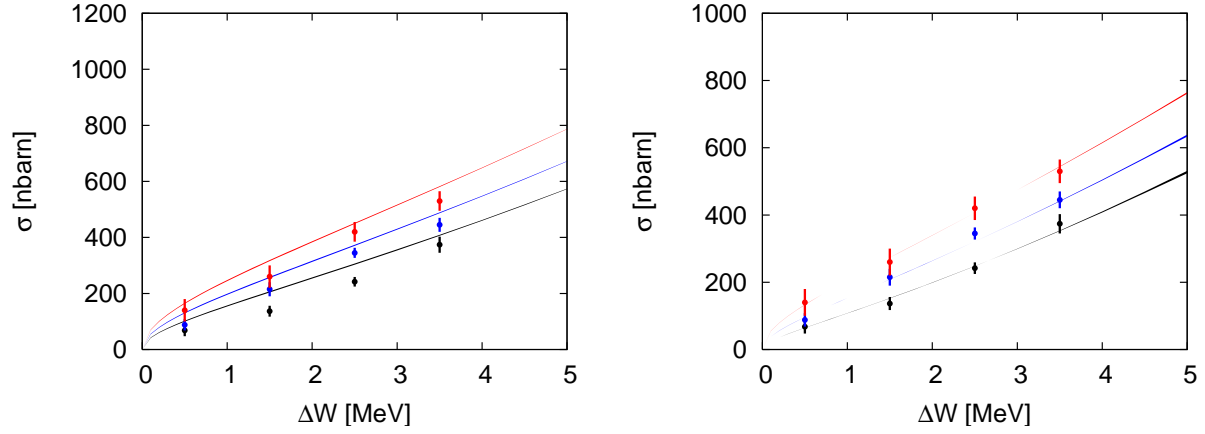


Fig. 10. Left panel: Total cross section as a function of ΔW for three different values of the photon polarization in comparison to the MAMI data [1] for fit 1 and the NNLO wave functions. The upper/middle/lower band corresponds to the largest/medium/smallest value of ε . Right panel: Same for fit 2.

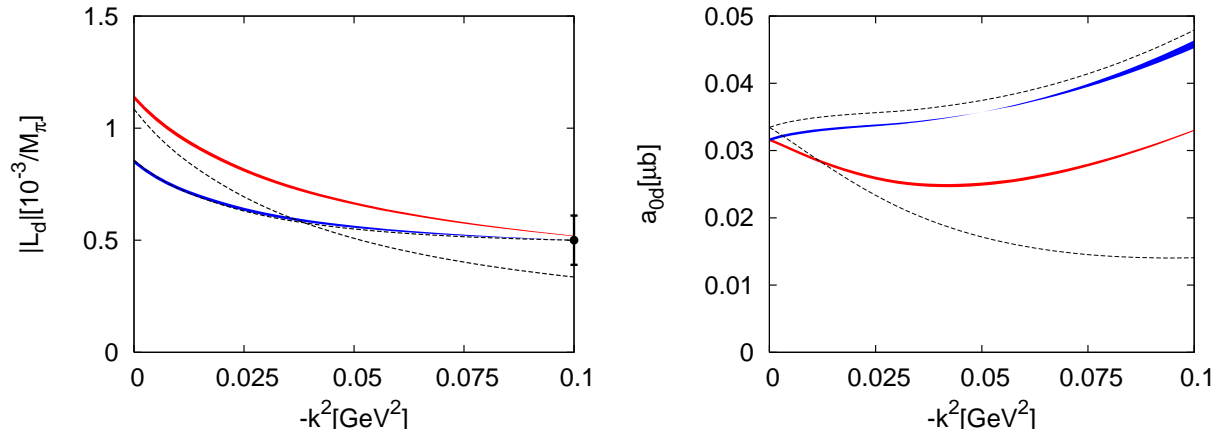


Fig. 11. Fits with varying four-nucleon LECs. Left panel: Threshold multipole $|L_d|$ as a function of the photon virtuality in comparison to the electroproduction data from MAMI [1]. The sign of the experimental result for L_d is taken to agree with the theoretical prediction. The blue (upper)/red (lower) band refers to fit 1,2, in order. Right panel: The S-wave cross section a_{0d} as a function of the photon virtuality. The solid bands give the range obtained with the fourth order three-body corrections, dashed lines show the third order tb results of [3].